

Measurement of the two neutrino double beta decay half-life of Zr-96 and search for associated neutrinoless processes with the NEMO-3 detector

J. Argyriades^a, R. Arnold^b, C. Augier^a, J. Baker^c, A.S. Barabash^c, A. Basharina-Freshvilleⁱ, M. Bongrand^a, G. Broudin-Bay^{g,f}, V. Brudanin^h, A.J. Caffrey^c, A. Chaponⁿ, E. Chauveau^{g,f}, Z. Daraktchievaⁱ, D. Durandⁿ, V. Egorov^h, N. Fatemi-Ghomi^j, R. Flackⁱ, B. Guillonⁿ, Ph. Hubert^{g,f}, S. Jullian^a, M. Kauer^{i,*}, S. Kingⁱ, A. Klimenko^h, O. Kochetov^h, S.I. Konovalov^c, V. Kovalenko^h, D. Lalanne^a, T. Lamhamdi^k, K. Lang^l, Y. Lemièrèⁿ, C. Longuemareⁿ, G. Lutter^{g,f}, F. Mamedov^m, Ch. Marquet^{g,f}, J. Martin-Albo^o, F. Maugerⁿ, A. Nachab^{g,f}, I. Nasteval^j, I. Nemchenok^h, C.H. Nguyen^{g,f,w}, F. Nova^p, P. Novella^o, H. Ohsumi^q, R.B. Pahlka^l, F. Perrot^{g,f}, F. Piquemal^{g,f}, J.L. Reyss^r, J.S. Ricol^{g,f}, R. Saakyanⁱ, X. Sarazin^a, Yu. Shitov^h, L. Simard^a, F. Šimkovic^s, A. Smolnikov^h, S. Snow^j, S. Söldner-Rembold^j, I. Štekl^m, C.S. Sutton^u, G. Szklarza^a, J. Thomasⁱ, V. Timkin^h, V.I. Tretyak^{h,b}, V. Umatov^c, L. Vála^m, I. Vanyushin^c, V. Vasilievⁱ, V. Vorobel^v, Ts. Vylov^h

(The NEMO-3 Collaboration)

^aLAL, Université Paris-Sud 11, CNRS/IN2P3, F-91405 Orsay, France

^bIPHC, Université de Strasbourg, CNRS/IN2P3, F-67037 Strasbourg, France

^cINL, Idaho National Laboratory, 83415 Idaho Falls, USA

^dINR, Institute of Nuclear Research, MSP 03680 Kyiv, Ukraine

^eITEP, Institute of Theoretical and Experimental Physics, 117259 Moscow, Russia

^fCNRS/IN2P3, Centre d' Etudes Nucléaires de Bordeaux Gradignan, UMR5797, F-33175 Gradignan, France

^gUniversité Bordeaux, CENBG, UMR 5797, F-33175 Gradignan, France

^hJINR, Joint Institute for Nuclear Research, 141980 Dubna, Russia

ⁱUniversity College London, WC1E 6BT London, United Kingdom

^jUniversity of Manchester, M13 9PL Manchester, United Kingdom

^kUSMBA, Université Sidi Mohamed Ben Abdellah, 30000 Fes, Morocco

^lUniversity of Texas at Austin, 78712-0264 Austin, Texas, USA

^mIEAP, Czech Technical University in Prague, CZ-12800 Prague, Czech Republic

ⁿLPC, ENSICAEN, Université de Caen, CNRS/IN2P3, F-14032 Caen, France

^oIFIC, CSIC - Universitat de Valencia, Valencia, Spain

^pUniversitat Autònoma Barcelona, Barcelona, Spain

^qSaga University, Saga 840-8502, Japan

^rLSCE, CNRS, F-91190 Gif-sur-Yvette, France

^sFMFI, Comenius University, SK-842 48 Bratislava, Slovakia

^tJyväskylä University, 40351 Jyväskylä, Finland

^uMHC, Mount Holyoke College, 01075 South Hadley, Massachusetts, USA

^vCharles University in Prague, Faculty of Mathematics and Physics, CZ-12116 Prague, Czech Republic

^wHanoi University of Science, Hanoi, Vietnam

Abstract

Using 1221 days of data from the NEMO-3 detector, the measurement of ^{96}Zr $2\nu\beta\beta$ decay half-life is $T_{1/2}^{2\nu} = [2.35 \pm 0.14(\text{stat}) \pm 0.19(\text{syst})] \times 10^{19}$ yr. Different characteristics of the final state electrons have been studied, such as the energy sum, individual electron energy, and angular distribution. The 2ν nuclear matrix element is extracted using the measured $2\nu\beta\beta$ half-life and is $M^{2\nu} = 0.049 \pm 0.003$. A 90% CL limit is set on the $0\nu\beta\beta$ decay half-life of $T_{1/2}^{0\nu} > 9.2 \times 10^{21}$ yr corresponding to a limit on the effective Majorana neutrino mass of $\langle m_{\beta\beta} \rangle < 7.2 - 19.5$ eV. Limits on other mechanisms of $0\nu\beta\beta$ decay have also been set.

Key words: double beta decay, Zr-96, zirconium, NEMO 3, neutrino

*Corresponding author

Email addresses: kauer@hep.ucl.ac.uk (M. Kauer)

Preprint submitted to Nuclear Physics A

July 21, 2022

1. Introduction

The recent observation of neutrino flavor oscillations and the resulting measurements of the neutrino mass squared differences [1] have motivated renewed experimental efforts to measure the absolute neutrino mass. The fundamental Dirac or Majorana [2] nature of the neutrino also remains indeterminate. Neutrinoless double beta decay ($0\nu\beta\beta$) is the only practical means of determining the nature of the neutrino and one of the most sensitive probes of its absolute mass. The mechanism most commonly discussed is shown in Figure 1 in which a light Majorana neutrino is exchanged [3]. The half-life in this case is given by

$$[T_{1/2}^{0\nu}]^{-1} = G^{0\nu} |M^{0\nu}|^2 \langle m_{\beta\beta} \rangle^2, \quad (1)$$

where $G^{0\nu}$ is the precisely calculable phase-space factor (proportional to $Q_{\beta\beta}^5$), $M^{0\nu}$ is the nuclear matrix element and $\langle m_{\beta\beta} \rangle$ is the effective Majorana neutrino mass. Other possible mechanisms for $0\nu\beta\beta$ include, for example, right-handed currents, Majoron emission and R-parity violating supersymmetry. In all mechanisms, the $0\nu\beta\beta$ process violates lepton number and is a direct probe for physics beyond the Standard Model.

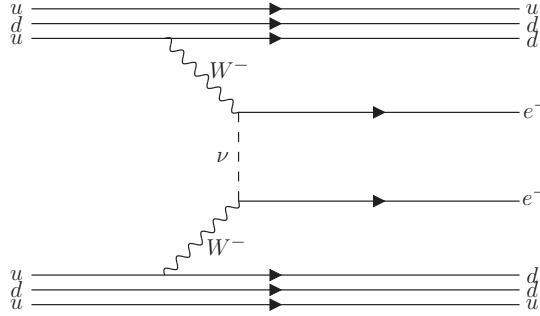


Figure 1: Feynman diagram for $0\nu\beta\beta$ decay via light Majorana neutrino exchange.

Measurement of the $2\nu\beta\beta$ process is important because it is an irreducible background component to 0ν mechanisms. Double beta decay ($2\nu\beta\beta$) allows experimental determination of the NME for this process ($M^{2\nu}$), which leads to the development of theoretical schemes for NME calculations for $2\nu\beta\beta$ and $0\nu\beta\beta$ [4, 5, 6]. The precision with which the lepton number violating parameter, such as $\langle m_{\beta\beta} \rangle$, can be measured depends crucially on knowledge of $M^{0\nu}$. Presented here are the results of observations of ^{96}Zr obtained with the NEMO-3 tracking plus calorimeter detector.

2. NEMO-3 Experimental Apparatus

A detailed description of the NEMO-3 detector and its performance can be found in [7], while the most salient properties are mentioned here. The detector is located in the Modane Underground Laboratory (LSM) 4800 meters water equivalent below ground and has been acquiring data since February 2003. It is a cylindrical detector ($\varnothing 5 \times 2.5$ m) holding 10 kg of enriched isotopes. The tracking volume contains ~ 6000 drift cells operating in Geiger mode (Geiger cells) enclosed by ~ 2000 polystyrene scintillator blocks making up the calorimeter. The detector is enclosed in a solenoid which generates a 25 Gauss magnetic field parallel to the Geiger cells. The transverse and longitudinal resolution of the tracker is 0.6 mm and 0.3 cm (σ) respectively. The calorimeter energy resolution and timing resolution is 14–17% (FWHM at 1 MeV) and 250 ps (σ at 1 MeV) respectively.

The majority of the $\beta\beta$ isotope mass is ^{100}Mo but other isotopes include ^{82}Se , ^{116}Cd , ^{130}Te , ^{150}Nd , ^{96}Zr , and ^{48}Ca . The experimental signature of $0\nu\beta\beta$ is two electrons with the energy sum equaling the $Q_{\beta\beta}$ of the decay. ^{96}Zr is of particular interest due to its high $Q_{\beta\beta} = 3350.0 \pm 3.5$ keV which is greater than the decay energies of most contributing background sources, and the large phase-space factor which is proportional to $Q_{\beta\beta}^5$. The total mass of the enriched ZrO_2 is 22.0 g of which 9.4 ± 0.2 g is ^{96}Zr [7]. NEMO-3 results thus far are published in [8, 9, 10, 11].

3. Event Topology and Particle Identification

The NEMO-3 detector is capable of sophisticated particle identification and event topology reconstruction. Electrons and positrons produce signals in both the calorimeter and Geiger cell tracker, while photons only signal the calorimeter. Due to the 25 Gauss magnetic field permeating the detector volume, the electron and positron discrimination efficiency is 97% at 1 MeV. Alpha particles (α) are identified by the short distance (~ 20 cm) they travel before quenching in the gas volume of the Geiger cells. Crossing electrons (an electron crossing the whole tracker volume and source foil to mimic a $\beta\beta$ event) are identified by the time-of-flight information from the two signaled calorimeter blocks. The event topologies studied in this analysis include the single electron channel ($1e$), the electron plus gamma channel ($e\gamma$), and the two electron channel (ee).

4. Backgrounds in NEMO-3

Studies have been carried out to identify the activities of the contributing backgrounds to NEMO-3 [12]. The backgrounds are categorized as “internal” or “external.” Internal backgrounds include isotopes decaying from within the source foil mimicking a $\beta\beta$ decay via Møller scattering, β decay with internal conversion, or β decay with Compton scattering of the de-excitation photon. Each of the seven $\beta\beta$ isotopes being measured at NEMO-3 has specific dominant internal backgrounds. External backgrounds include all decays originating from outside the source foil but still mimic a $\beta\beta$ event signature via double Compton scattering, Compton plus Møller scattering, or pair production. Charge identification via track curvature in the magnetic field tags pair production events. The two most detrimental contributors are ^{214}Bi and ^{208}Tl with respective Q_β values of 3.270 MeV and 4.992 MeV. NEMO-3 component and source foil activities were measured with a high purity germanium detector (HPGe) and were subject to a selection process to optimize radio-purity.

4.1. Radon (^{222}Rn)

The first data acquisition period (Feb 2003 – Oct 2004) is referred to as Phase-I and had a relatively high (1200 mBq) level of radon in the tracking volume. Radon (^{222}Rn) is particularly disruptive because it is a noble gas and its half-life of 3.82 days provides enough time to be outgassed from the surrounding rock and permeate the detector volume. Supporting evidence suggests [13] that a large fraction (87%) of α decay daughters are positively charged and are attracted to electrostatically negative and electrically grounded surfaces. NEMO-3 data are consistent with the radon daughters being deposited on the surfaces of reflecting wrapping around the scintillators, the drift cell cathode wires and the source foils [12].

The second data acquisition period (Nov 2004 – Dec 2007) is referred to as Phase-II and began with the installation of a radon purification facility to inject a flow of pure air around the detector. The purification facility suppresses the radon concentration in the immediate proximity of the detector by a factor of ~ 1000 . However, the outgassing of detector components releasing radon due to their internal contamination with the $^{238}\text{U} - ^{226}\text{Ra}$ chain leads to a smaller reduction factor inside the detector. The radon activity in the tracker volume decreased from 1.2 Bq in Phase-I to 0.2 Bq in Phase-II.

5. Data Analysis

All background and signal events are simulated with DECAY0 [14] which accurately reproduces energy and angular distributions of particles emitted in radioactive decays including $2\nu\beta\beta$ and theoretical $0\nu\beta\beta$ mechanisms. All generated particles are propagated through a full GEANT-3.21 [15] description of the detector. The simulated Monte Carlo (MC) events are in the same format as the raw data from the NEMO-3 detector and both MC and real data are reconstructed with the same software package.

5.1. Background Identification

One can measure the activities of the various background isotopes by the event topologies and kinematics determined by the selection criteria. All background isotopes are measured with the single electron ($1e$) and electron plus gamma ($e\gamma$) channels. A global analysis of the external background is discussed in [12]. ^{208}Tl and ^{214}Bi were independently measured using $e\gamma\gamma$, $e\gamma\gamma\gamma$, and $e\alpha$ channels. The so-called “external background model” has been tested and validated using the dedicated sectors of ultra-pure Cu and Te foils in NEMO-3.

Limits have been placed on the internal background activities of ^{96}Zr by a high purity germanium (HPGe) detector, but ultimately the internal background activities are measured with the NEMO-3 apparatus. Internal background activities are measured in the $1e$ and $e\gamma$ channels. The $1e$ selection criteria are the following: one negatively charged particle track with length greater than 50 cm originating from the ^{96}Zr source foil and terminating at a scintillator, and an energy deposit > 500 keV in the scintillator associated with the track. The $e\gamma$ selection criteria are the following: one negatively charged particle track with length greater than 50 cm originating from the ^{96}Zr source foil and terminating at a scintillator, an energy deposit > 200 keV in the scintillator associated with the track, an energy deposit > 200 keV in a separate scintillator with no associated track, the cosine of the angle between the electron and gamma must be < 0.9 , and the time-of-flight information must be consistent with the electron and gamma originating from the same point in the source foil. In both the $1e$ and $e\gamma$ channels (for quality control of the reconstructed track) we require at least one triggered Geiger cell in first two layers closest to the source foil and less than 3 triggered Geiger cells that are not associated with the reconstructed track.

The internal background activities are distinguished and measured due to contrasting Q_β values and $1e$ and $e\gamma$ energy spectra of the isotopes. Equilibrium within a decay chain implies specific isotope activities to be correlated. ^{228}Ac , ^{212}Bi , and ^{208}Tl are part of the ^{232}Th chain and separated by short half-lives, therefore ^{228}Ac and ^{212}Bi activities are set equal and ^{208}Tl is set to its branching ratio of 36%. ^{214}Bi and ^{214}Pb belong to the ^{238}U chain and are set equal. ^{234m}Pa is also part of the ^{238}U decay chain but equilibrium with ^{214}Bi cannot be assumed due to the large half-life of the intermediate isotope ^{226}Ra . Within this background model, contributions from the above isotopes to the $1e$ and $e\gamma$ channels have been fitted to experimental data over the entire energy region leaving the activities of the isotopes floating. Figure 2 shows the goodness of fit of the $1e$ channel and has a $\chi^2 = 49.6/45$. Figure 3 shows the $e\gamma$ channel and has a $\chi^2 = 29.5/23$. The individual and summed energy distributions of electrons and gammas as well as the angular distribution between them are plotted. The measurements of the internal ^{96}Zr contaminations obtained in the $1e$ and $e\gamma$ channels compared with previously obtained HPGe limits in Table 1 provide a cross-check for the NEMO-3 measurements. The obtained numbers are in agreement with the ^{214}Bi and ^{208}Tl activities (0.17 ± 0.05 and 0.08 ± 0.01 mBq respectively) reported in [12] where more restrictive energy intervals and different event topologies were used to identify signatures of the isotopes.

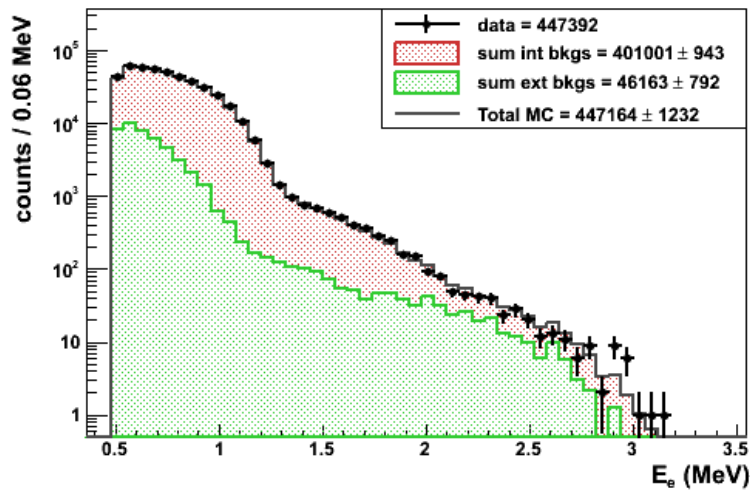


Figure 2: Distribution of energies in the $1e$ channel. The background contributions are divided into 2 sub-groups of summed internal (int) and external (ext) components.

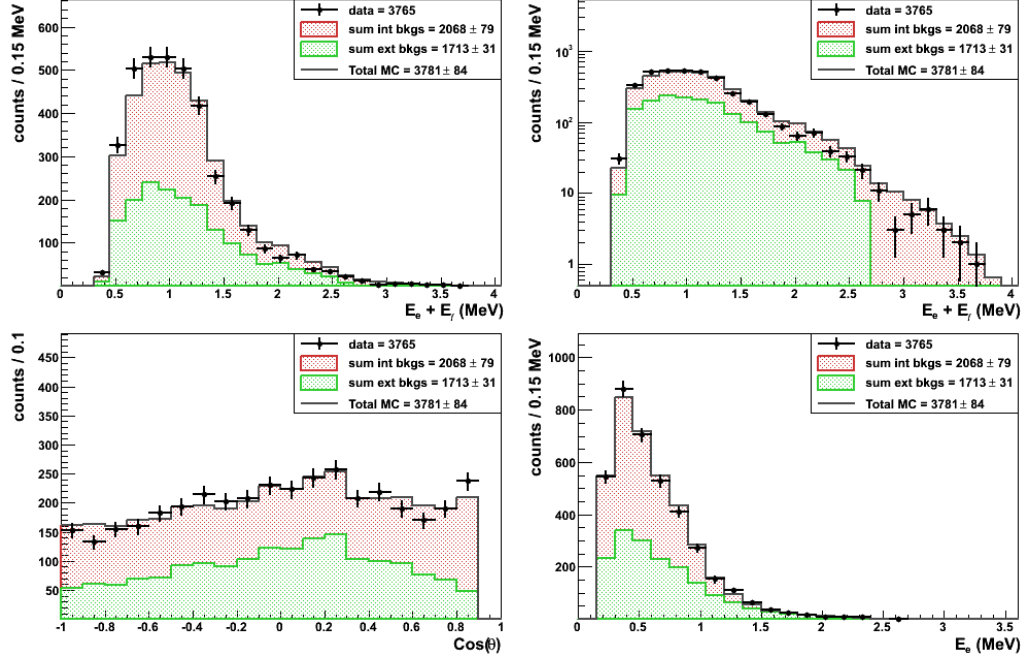


Figure 3: The $e\gamma$ channel displaying the summed energy $E_e + E_\gamma$ (top-left and top-right), the angular distribution between the electron and gamma (bottom-left), and the energy of the electron E_e (bottom-right). As in Figure 2, the background contributions are divided into 2 sub-groups of summed internal (int) and external (ext) components.

Table 1: Internal contamination of the ^{96}Zr foil measured with NEMO-3 in the $1e$ and $e\gamma$ channels under the assumptions of the background model described in 5.1. The NEMO-3 measurements are compared to HPGe limits at 95% confidence level.

Isotope	NEMO-3 (mBq)	HPGe (mBq)
^{228}Ac	0.25 ± 0.02	< 0.75
^{212}Bi	0.25 ± 0.02	< 0.75
^{208}Tl	0.091 ± 0.007	< 0.23
^{214}Bi	0.19 ± 0.02	< 0.45
^{214}Pb	0.19 ± 0.02	< 0.45
^{40}K	19.7 ± 0.1	< 19
^{234m}Pa	0.49 ± 0.01	< 6.6

The adjacent $\beta\beta$ source isotopes (^{150}Nd and ^{48}Ca) and their associated internal backgrounds contribute events that pass the ^{96}Zr selection criteria due to the positional resolution of the Geiger cell tracker and accuracy of the reconstructed event vertex. These events have been studied and contribute $\sim 1\%$ in the $1e$ channel and $\sim 7\%$ in the $e\gamma$ channel and are included in the background description for ^{96}Zr .

6. Results

6.1. $2\nu\beta\beta$ Decay

The selection criteria for ee events are the following: two negatively charged particle tracks with lengths greater than 30 cm, both tracks originating from the ^{96}Zr foil and terminating at independent scintillators, energy deposits > 200 keV in the scintillators associated with the tracks, each track has at least one triggered Geiger cell in first two layers closest to the source foil, and the time-of-flight information must be consistent with the two electrons originating from the same point on the source foil.

The distributions of the energy sum of the two electrons, energies of the individual electrons, and the angle between two electrons are shown in Figure 4. 898 data events have been selected after 1221 days of data taking with a total expected background of 439 ± 7 events. A maximized binned log-likelihood fit to the energy sum spectrum is performed to estimate the $2\nu\beta\beta$ signal contribution. The likelihood fit predicts 428 ± 26 signal events (signal-to-background of 0.98) with a 7.7% efficiency. The breakdown of individual background contributions is shown in Table 2.

Table 2: The number of events expected for the ^{96}Zr internal and external backgrounds in the ee channel for 1221 days of runtime.

Background	Expected N_{bkg}
^{228}Ac	11.1 ± 0.9
^{212}Bi	9.6 ± 0.7
^{208}Tl	9.3 ± 0.7
^{214}Bi	22.8 ± 2.5
^{214}Pb	3.3 ± 0.4
^{40}K	280.0 ± 2.4
^{234m}Pa	38.3 ± 0.7
^{48}Ca internals	0.0 ± 0.0
^{150}Nd internals	38.6 ± 2.9
External	25.5 ± 5.2
Total	438.5 ± 7.0

The systematic error on the $2\nu\beta\beta$ measurement has been investigated. The main contribution is from the error on the tracking chamber resolution and track reconstruction efficiency. There is a 2% uncertainty in the mass of ^{96}Zr . The precision of the energy calibration of the calorimeter is 1% and the effect was determined by coherently changing the gain of the photomultipliers $\pm 1\%$ and observing the change in the half-life measurement. The uncertainty on the total activity of all backgrounds is 10% [12]. The effect of the background uncertainty on the measured half-life was determined by fluctuating the total activity and observing the change in half-life. ^{40}K is the dominant background in the ee channel and a systematic effect is observed by changing the energy window of the likelihood fit to exclude energy sums below 1.1 MeV. These systematic uncertainties are listed in Table 3.

The final result for the $2\nu\beta\beta$ half-life of ^{96}Zr including statistical and systematic errors is

$$T_{1/2}^{2\nu} = [2.35 \pm 0.14(\text{stat}) \pm 0.19(\text{syst})] \times 10^{19} \text{ yr}. \quad (2)$$

For comparison, (2) is consistent and more precise than the previous direct measurement $(2.1_{-0.4}^{+0.8}(\text{stat}) \pm 0.2(\text{syst})) \times 10^{19} \text{ yr}$ [16].

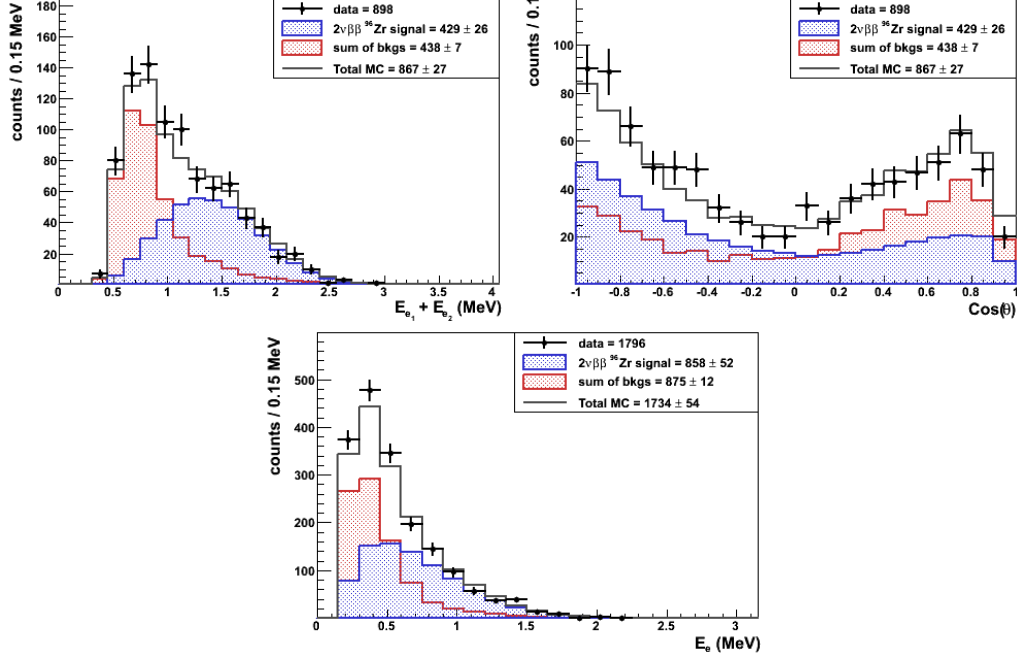


Figure 4: The energy sum of both electrons $E_{e1} + E_{e2}$ (top-left), angular distribution $\cos(\theta)$ (top-right), and individual electron energy E_e (bottom-center) for 1221 days of runtime in the ee channel. The data are described by the sum of the expected backgrounds from MC and the $2\nu\beta\beta$ signal from the maximized log-likelihood fit.

Table 3: Summary of systematic errors pertaining to the $2\nu\beta\beta$ measurement of ^{96}Zr .

Description	Syst. Error (%)	
the tracker and reconstruction	$\pm 5.0\%$	[7]
the mass of ^{96}Zr	$\pm 2.0\%$	[7]
a $\pm 1\%$ energy calibration precision	$+2.9\%, -2.2\%$	
a $\pm 10\%$ total background precision	$+4.9\%, -4.8\%$	
the likelihood fit energy window	$+2.2\%, -0.3\%$	
Total	$+8.2\%, -7.5\%$	

6.2. $0\nu\beta\beta$ Decay (neutrino mass mechanism)

Limits on 0ν processes are evaluated using a binned log-likelihood ratio (LLR) test statistic [17]. Signal-plus-background and background-only hypotheses are defined and populated with simulated outcomes via Poisson statistics. The confidence level on the signal (CL_s) is defined as $CL_s = CL_{s+b}/CL_b$, where CL_{s+b} and CL_b are the confidence levels of the signal-plus-background and background-only hypotheses respectively. The limit is found by scaling the signal until CL_s reaches the 90% level. The detection efficiency for observing the $0\nu\beta\beta$ decay is 20.3% and the limit at the 90% CL (Figure 5) is

$$T_{1/2}^{0\nu} > 9.2 \times 10^{21} \text{ yr}. \quad (3)$$

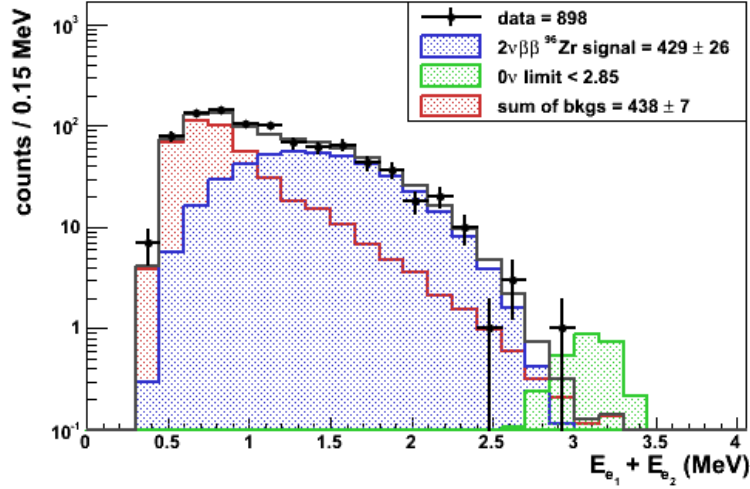


Figure 5: Energy sum distribution of two electrons $E_{e_1} + E_{e_2}$ for 1221 days of runtime. The data are described by the sum of the expected backgrounds from MC, the measured $2\nu\beta\beta$ signal, and the limit on $0\nu\beta\beta$ at 90% CL using the log-likelihood ratio test statistic method described in 6.2. The 0ν histogram is not included in the total MC (dark-grey)

6.3. Other $0\nu\beta\beta$ Transitions

More exotic mechanisms include 0ν excited states, right-handed currents (RHC) and the emission of one or two Majoron particles (χ^0). The term “Majoron” is generally used to describe massless or light bosons which weakly couple to neutrinos. The various Majoron models are referred to by their spectral index n which determines the dependence of the phase space on the energy released in the decay as $G^{0\nu} \propto (Q_{\beta\beta} - T)^n$, where T is the sum of the kinetic energies of the electrons emitted in the decay. The standard model $2\nu\beta\beta$ decay has $n = 5$. For single Majoron emission ($\chi^0\beta\beta$) $n = 1$ [18, 19], for double Majoron emission ($\chi^0\chi^0\beta\beta$) $n = 3$ or $n = 7$, [20, 21, 18] and for the “bulk” Majoron in the context of the “brane-bulk” scenario $n = 2$ [22]. The limits have been obtained using the binned log-likelihood ratio test statistic method described in 6.2. The results are presented in Tables 4 and 5.

Table 4: Summary of half-life limits $T_{1/2}$ (yr.) evaluated at the 90% CL for $0\nu\beta\beta$ mechanisms where $0_{gs}^+(\langle m_{\beta\beta} \rangle)$ is the standard $0\nu\beta\beta$ decay to the ground state, $0_1^+(\langle m_{\beta\beta} \rangle)$ is the first excited state, $0_{gs}^+(\text{RHC}; \lambda)$ is the right-handed current decay to ground state and $2_1^+(\text{RHC}; \lambda)$ is the first excited state. The bottom line is the previous best limit presented for comparison.

$0\nu\beta\beta$			
$0_{gs}^+(\langle m_{\beta\beta} \rangle)$	$0_1^+(\langle m_{\beta\beta} \rangle)$	$0_{gs}^+(\text{RHC}; \lambda)$	$2_1^+(\text{RHC}; \lambda)$
9.2×10^{21}	2.2×10^{20}	5.1×10^{21}	9.1×10^{20}
1.0×10^{21} [16]	6.8×10^{19} [23]	-	3.9×10^{20} [16]

Naively one would expect the mass mechanism and RHC limit to be identical because they have the same summed energy spectrum, but due to the asymmetrical energies and small angle ($\cos \theta \sim 1$) between the emitted electrons in the RHC process, detector efficiencies decrease the RHC acceptance.

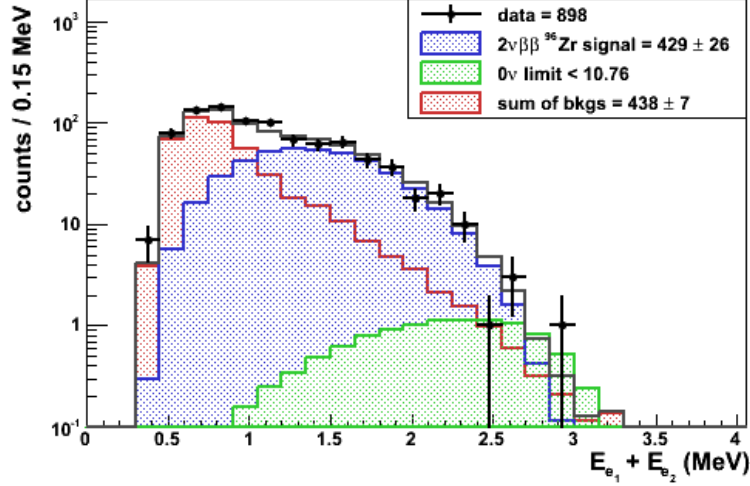


Figure 6: Energy sum distribution of two electrons $E_{e_1} + E_{e_2}$ for 1221 days of runtime. The data are described by the sum of the expected backgrounds from MC, the measured $2\nu\beta\beta$ signal, and the limit on $n = 1$ Majoron emission at 90% CL using the log-likelihood ratio test statistic method described in 6.2. The 0ν histogram is not included in the total MC (dark-grey)

Table 5: Summary of half-life limits $T_{1/2}$ (yr.) evaluated at the 90% CL for Majoron emission decay mechanisms. The spectral index (n) for the Majoron modes refers to the dependence of $G^{0\nu} \propto (Q_{\beta\beta} - T)^n$ where T is the electrons' kinetic energy sum. The bottom line is the previous best limit presented for comparison.

Majoron			
$n = 1$	$n = 2$	$n = 3$	$n = 7$
1.9×10^{21}	9.9×10^{20}	5.8×10^{20}	1.1×10^{20}
3.5×10^{20} [24]	-	6.3×10^{19} [24]	5.1×10^{19} [24]

7. Discussion

7.1. 2ν NME

The largest uncertainty in the effective Majorana mass determination is due to the uncertainty of the $0\nu\beta\beta$ NME ($M^{0\nu}$). It is still difficult to calculate the NMEs for ^{96}Zr and currently there are no large-scale shell model calculations (see review [25]). The current models for the $M^{0\nu}$ computation of ^{96}Zr are the quasi-particle random-phase approximation (QRPA) and the renormalized (RQRPA) [4, 5, 6], but unfortunately cannot precisely predict $M^{2\nu}$ due to strong dependence on the unknown parameter g_{pp} (particle-particle coupling). In fact, extracted experimental values of $M^{2\nu}$ are needed to fix g_{pp} which is used for the $M^{0\nu}$ computations. Two values for the parameter g_A are generally agreed upon and the NME is computed using both $g_A = 1.0$ and $g_A = 1.25$. Recently a new approach (Projected Hartree-Fock-Bogoliubov – PHFB model) was developed [26, 27, 28] which can predict the $M^{2\nu}$ and $M^{0\nu}$ values.

Using the measured value of the ^{96}Zr $2\nu\beta\beta$ half-life (2) we extract the experimental value of the corresponding NME according to the formula

$$[T_{1/2}^{2\nu}]^{-1} = G^{2\nu} |M^{2\nu}|^2, \quad (4)$$

where $G^{2\nu} = 1.8 \times 10^{-17} \text{ yr}^{-1}$ is the known phase space factor [25], which yields the result

$$M^{2\nu} = 0.049 \pm 0.003. \quad (5)$$

One can compare this (5) value with the calculated value, $M^{2\nu} = 0.058$ [26]. The obtained precise value for $M^{2\nu}$ will be used to fix g_{pp} parameter and improve the $M^{0\nu}$ calculations for ^{96}Zr .

7.2. Majorana Neutrino Mass

The limit on the $0\nu\beta\beta$ half-life (3) is used to calculate an upper bound on the effective Majorana neutrino mass, $\langle m_{\beta\beta} \rangle$ from (1). Using the NME computed in [4] (QRPA) and [5, 6] (QRPA and RQRPA) the following limits on the effective Majorana neutrino mass are obtained. The range is due to the $M^{0\nu}$ uncertainty:

$$\langle m_{\beta\beta} \rangle < 7.2 - 8.2 \text{ eV} \quad (\text{NME from [4]}), \quad (6)$$

$$\langle m_{\beta\beta} \rangle < 11.0 - 19.5 \text{ eV} \quad (\text{NME from [5, 6]}). \quad (7)$$

Using the NME from [27] (PHFB approach) we obtain $\langle m_{\beta\beta} \rangle < 15.1 \text{ eV}$.

7.3. Majoron-Neutrino Coupling

A limit on the Majoron to neutrino coupling $\langle g_{ee} \rangle$ is extracted for the most commonly discussed mechanism with $n = 1$ (Figure 6) from

$$[T_{1/2}^{0\nu\chi^0}]^{-1} = G^{0\nu\chi^0} |M^{0\nu\chi^0}|^2 \langle g_{ee} \rangle^2. \quad (8)$$

The Majoron matrix element $M^{0\nu\chi^0}$ is identical to that of the mass mechanism ($M^{0\nu}$) and using NME from [4] (QRPA) and [5, 6] (QRPA and RQRPA) the following limits on the Majoron coupling are obtained. The range is due to the $M^{0\nu\chi^0}$ uncertainty:

$$\langle g_{ee} \rangle < (1.5 - 2.1) \times 10^{-4} \quad (\text{NME from [4]}), \quad (9)$$

$$\langle g_{ee} \rangle < (3.3 - 5.7) \times 10^{-4} \quad (\text{NME from [5, 6]}). \quad (10)$$

Using the NME from [27] (PHFB approach) we obtain $\langle g_{ee} \rangle < 4.4 \times 10^{-4}$. For mechanisms $n = 2, 3$, and 7 our limits are comparable with the best present limits obtained with other nuclei [29].

7.4. G_F Time Variation Hypothesis

It has been suggested in [30, 31] that observed differences in half-lives of $\beta\beta$ isotopes obtained in geochemical experiments with samples of different age could be related to time dependence of the Fermi constant G_F . Due to the stronger dependence on the Fermi constant (G_F^4 rather than G_F^2), $\beta\beta$ decay offers a better sensitivity than single β decay studies. The $^{96}\text{Zr} - ^{96}\text{Mo}$ transition is of particular interest since the daughter element is not a gas thus eliminating the main systematic error of the geochemical measurements. A comparison between the half-lives obtained with ancient zircon (ZrSiO_4) minerals characterizing the decay rate in the past with present day $\beta\beta$ decay rates obtained in a direct experiment like the one presented here allows the hypothesis to be probed with a high precision.

A previous geochemical measurement carried out in 1992 with a $1.7 \times 10^9 \text{ yr}$ old zircon yielded a $2\nu\beta\beta$ half-life of $(3.9 \pm 0.9) \times 10^{19} \text{ yr}$ [32]. An independent measurement was performed in 2001 with a number of zircons aged $\sim 1.8 \times 10^9 \text{ yr}$ and a half-life of $(0.94 \pm 0.32) \times 10^{19} \text{ yr}$ was measured [33]. The measurement presented in this paper (2) lies between the two geochemical measurements. More accurate studies of minerals of different age are needed in order to probe the G_F time variation hypothesis with high precision.

8. Summary

The most precise measurement of the $2\nu\beta\beta$ decay half-life of ^{96}Zr to date has been presented including the characteristics of the final state electrons (energy sum, individual electron energy, and angular distribution). The presented limit on the $0\nu\beta\beta$ half-life (3) is an order of magnitude higher compared to the previous result [16]. The presented limits on other 0ν processes are the best to date. The high $Q_{\beta\beta}$ value, hence large phase-space of ^{96}Zr , makes it an excellent choice for the study of $0\nu\beta\beta$ decay if the enrichment of this isotope in large quantities proves to be feasible.

Acknowledgment

We thank the staff at the Modane Underground Laboratory for their technical assistance in running the NEMO-3 experiment and Vladimir I. Tretyak for providing the Monte Carlo event generator (DECAY0). We acknowledge support by the Grants Agencies of the Czech Republic, RFBR (Russia), STFC (UK), and NSF (USA).

References

- [1] G. L. Fogli, E. Lisi, A. Marrone, and A. Palazzo. Global analysis of three-flavor neutrino masses and mixings. *Prog. Part. Nucl. Phys.*, 57:742–795, 2006, hep-ph/0506083.
- [2] Ettore Majorana. Theory of the Symmetry of Electrons and Positrons. *Nuovo Cim.*, 14:171–184, 1937.
- [3] W. H. Furry. On transition probabilities in double beta-disintegration. *Phys. Rev.*, 56:1184–1193, 1939.
- [4] Markus Kortelainen and Jouni Suhonen. Nuclear matrix elements of neutrinoless double beta decay with improved short-range correlations. *Phys. Rev.*, C76:024315, 2007, nucl-th/0708.0115.
- [5] Fedor Simkovic, Amand Faessler, Vadim Rodin, Petr Vogel, and Jonathan Engel. Anatomy of nuclear matrix elements for neutrinoless double-beta decay. *Phys. Rev.*, C77:045503, 2008, nucl-th/0710.2055.
- [6] V. A. Rodin, A. Faessler, F. Simkovic, and P. Vogel. Assessment of uncertainties in QRPA 0nu beta beta decay nuclear matrix elements. *Nucl. Phys.*, A766:107–131, 2006, nucl-th/0706.4304.
- [7] R. Arnold et al. Technical design and performance of the NEMO 3 detector. *Nucl. Instrum. Meth.*, A536:79–122, 2005, physics/0402115.
- [8] R. Arnold et al. First results of the search of neutrinoless double beta decay with the NEMO 3 detector. *Phys. Rev. Lett.*, 95:182302, 2005, hep-ex/0507083.
- [9] R. Arnold et al. Limits on different Majoron decay modes of Mo-100 and Se-82 for neutrinoless double beta decays in the NEMO-3 experiment. *Nucl. Phys.*, A765:483–494, 2006, hep-ex/0601021.
- [10] R. Arnold et al. Measurement of double beta decay of Mo-100 to excited states in the NEMO 3 experiment. *Nucl. Phys.*, A781:209–226, 2007, hep-ex/0609058.
- [11] J. Argyriades et al. Measurement of the Double Beta Decay Half-life of 150-Nd and Search for Neutrinoless Decay Modes with the NEMO-3 Detector. 2008, hep-ex/0810.0248.
- [12] J. Argyriades et al. Measurement of the background in the NEMO 3 double beta decay experiment. 2009, nucl-ex/0903.2277.
- [13] P. Pagelkopf and J. Porstendorfer. Neutralisation rate and the fraction of the positive 218Po-clusters in air. *Atmospheric Environment*, 37:1057–1064(8), March 2003.
- [14] O. A. Ponkratenko, V. I. Tretyak, and Yu. G. Zdesenko. The Event generator DECAY4 for simulation of double beta processes and decay of radioactive nuclei. *Phys. Atom. Nucl.*, 63:1282–1287, 2000, nucl-ex/0104018.
- [15] R. Brun, F. Bruyant, M. Maire, A. C. McPherson, and P. Zanzuri. GEANT-3. 1987. CERN-DD/EE/84-1.
- [16] R. Arnold et al. Double beta decay of Zr-96. *Nucl. Phys.*, A658:299–312, 1999.
- [17] Thomas Junk. Confidence level computation for combining searches with small statistics. *Nucl. Instrum. Meth.*, A434:435–443, 1999, hep-ex/9902006.
- [18] R. N. Mohapatra and P. B. Pal. Massive neutrinos in physics and astrophysics. Second edition. *World Sci. Lect. Notes Phys.*, 60:1–397, 1998.
- [19] Z. G. Berezhiani, A. Yu. Smirnov, and J. W. F. Valle. Observable Majoron emission in neutrinoless double beta decay. *Phys. Lett.*, B291:99–105, 1992, hep-ph/9207209.
- [20] P. Bamert, C. P. Burgess, and R. N. Mohapatra. Multi-Majoron modes for neutrinoless double beta decay. *Nucl. Phys.*, B449:25–48, 1995, hep-ph/9412365.
- [21] R. N. Mohapatra and E. Takasugi. Neutrinoless Double Beta Decay with Double Majoron Emission. *Phys. Lett.*, B211:192, 1988.
- [22] R. N. Mohapatra, Abdel Perez-Lorezana, and C. A. de S Pires. Neutrino mass, bulk Majoron and neutrinoless double beta decay. *Phys. Lett.*, B491:143–147, 2000, hep-ph/0008158.
- [23] A. S. Barabash et al. Investigation of the Beta Beta decay of Zr-96 to excited states in Mo-96. *J. Phys.*, G22:487–496, 1996.
- [24] R. Arnold et al. Limits on different Majoron decay modes of Mo-100, Cd-116, Se-82 and Zr-96 for neutrinoless double beta decays in the NEMO-2 experiment. *Nucl. Phys.*, A678:341–352, 2000.
- [25] J. Suhonen and O. Civitarese. Weak-interaction and nuclear-structure aspects of nuclear double beta decay. *Phys. Rept.*, 300:123–214, 1998.
- [26] R. Chandra, J. Singh, P. K. Rath, P. K. Raina, and J. G. Hirsch. Two neutrino double beta decay of A=94 through A=110 nuclei for 0+ to 0+ transition. *Eur. Phys. J.*, A23:223–234, 2005, nucl-th/0405074.
- [27] K. Chaturvedi, R. Chandra, P. K. Rath, P. K. Raina, and J. G. Hirsch. Nuclear deformation and neutrinoless double-beta decay of Zr-94, Zr-96, Mo-98, Mo-100, Ru-104, Pd-110, Te-128, Te-130, and Nd-150 nuclei within a mechanism involving neutrino mass. *Phys. Rev.*, C78:054302, 2008.
- [28] R. Chandra, K. Chaturvedi, P. K. Rath, P. K. Raina, and J. G. Hirsch. Multipolar correlations and deformation effect on nuclear transition matrix elements of double-beta decay. 2009, nucl-th/0902.0658.
- [29] A. S. Barabash. Double beta decay: present status. 2008, hep-ex/0807.2948.
- [30] A. S. Barabash. Is the weak interaction constant really constant? *Czech. J. Phys.*, 50:455–461, 2000.
- [31] A. S. Barabash. Possible evidence of time variation of weak interaction constant from double beta decay experiments. *Astrophys. Space Sci.*, 283:607–612, 2003, nucl-ex/0210011.
- [32] A. Kawashima, A. Masuda, and K. Takahashi. Geochemical estimation of the halflife for the double beta decay of Zr-96. *Phys. Rev.*, C47:2452–2456, 1993.
- [33] Michael E. Wieser and John R. De Laeter. Evidence of the double beta decay of zirconium-96 measured in 1.8 x 10⁹ year-old zircons. *Phys. Rev.*, C64:024308, 2001.